

Physical limits of ultra-high-finesse optical cavities: Taming two-level systems of glassy metal oxides

H. R. Kong^{1,2} and K. S. Choi^{1,2,*}

¹*Institute for Quantum Computing and Department of Physics & Astronomy,
University of Waterloo, Waterloo, Ontario N2L 3G1, Canada*

²*Q-Block Computing Inc., Kitchener, Ontario N2C 2C8, Canada*

The framework of tunnelling states in amorphous media provides the dissipative mechanism that imposes fundamental limits on the performances of ultra-high-Q optical and microwave resonators. In the optical domain, however, the microscopic nature of the tunnelling states and their direct consequences to the optical losses have not been characterized. In this work, we examine the interplay between glassy physics and stoichiometric point defects of ultra-low-loss dielectric mirrors, with a focus on two-level systems of oxygen defects in metal oxide, Ta₂O₅. In the context of ultra-high-finesse optical cavities, we characterize the Urbach tail of Ta₂O₅ under thermal annealing and reactive oxygen plasma. For the first time, we microscopically resolve the individual oxygen point defects on the mirror surfaces and introduce laser-assisted annealing to selectively “cure” surface defects. By exploiting these techniques, we report the realization of ultra-high-finesse optical cavity with finesse $\mathcal{F} = 450,000$ and the absorption-scatter loss 0.1 ± 0.2 ppm at 852 nm.

I. INTRODUCTION

While mechanical properties of crystalline structure are well understood, amorphous media have more complex properties. Due to the extensive metastable states, glassy systems are prevented from equilibration to the thermal bath, and their structural organizations manifest bulk properties that can be measured by specific heat and thermal conductivity. The dynamical behaviour of amorphous (glassy) systems at low-temperature can be captured by the phenomenology of low-energy two-level systems (TLS) [1–4] that fluctuate and dissipate the spatial ordering of the glass. In this context, annealing could be thought of as a method to equilibrate their configurational states and to relax towards lower energies.

Since the 70s, the semiconductor industry and related areas have made a broad scope of studies around dielectric materials, with a focus of its dielectric loss that relates to the performance of field effect transistors [5, 6]. In the modern context, TLS of amorphous metal oxides is the limiting factor for the performances of gravitational wave detector and optical clocks by their coating brownian motion [7–11], and can also contribute to the optical losses for cavity quantum electrodynamics (QED) experiments [12]. The TLS in native oxide layers of active metals causes an increased micromotion for the trapped ions on surface traps [13] and limits the Q -factor of superconducting circuits with junction noise [14]. For ultra-high- Q optical resonators, structural organization of high-index metal oxides gives rise to bulk optical properties near the mobility edge from the extensive localized states that deform their optical density of states with a finite Urbach tail. In addition to the long-range order, interfacial local defects can dissipate and fluctuate the optical fields in high-finesse cavities over a spectral ex-

tent connected to their short-range ordering. The structural disorders pose a fundamental limit to the optical Q -factors of optical cavities and interferometers that can be attained by amorphous media. As a premier material for ultra-low-loss optical interferometers over the past decades, most studies in the optical domain have exclusively focused on the long-wavelength structural disorders of tantalum pentoxide (Ta₂O₅, hereafter referred as tantala) that give rise to the coating thermal noise of ultra-high-finesse optical resonators [9–11, 15–17]. However, the microscopic origins of the TLS and their direct manifestations to the optical losses are closely connected to the short-wavelength structural organization, and have not yet been characterized in any experiment.

In this work, we investigate the crucial role of amorphicity on the dielectric coatings of optical mirrors with a focus on tantala deposited by ion-beam sputtering (IBS). We perform ellipsometric measurements of the Urbach tails of ultra-low-loss optical films and investigate the thermal annealing and O₂ plasma treatments for the reduction of optical loss in the UV range. We also spatially resolve the individual oxygen point defects at the interfaces of bilayer quarter-wave stack for ultra-low-loss mirror with a high-resolution optical microscope, and confirm their defect states near the Fermi level 2.19 eV by photoluminescence emission spectroscopy. Importantly, we examine the oxygen vacancy as an optically active TLS that limits the optical Q -factor of ultra-high-finesse cavities in the near-infra-red (NIR) regime. We develop a microscopic technique of laser-assisted local annealing for the removal of the stoichiometric defects at the atomic level. By constructing ultra-high-finesse optical resonators, we observe the key role of oxygen vacancy to the mirror’s absorption-scatter (AS) losses. We thereby report the realization of a nearly defect-free ultra-high-finesse optical cavity for the recent many-body QED experiment [18] with optical finesse $\mathcal{F} = 445,000$ and $AS = 0.1 \pm 0.2$ ppm at 852 nm. Our result improves significantly upon the seminal work by Rempe *et al.* [12],

* kyung.choi@uwaterloo.ca

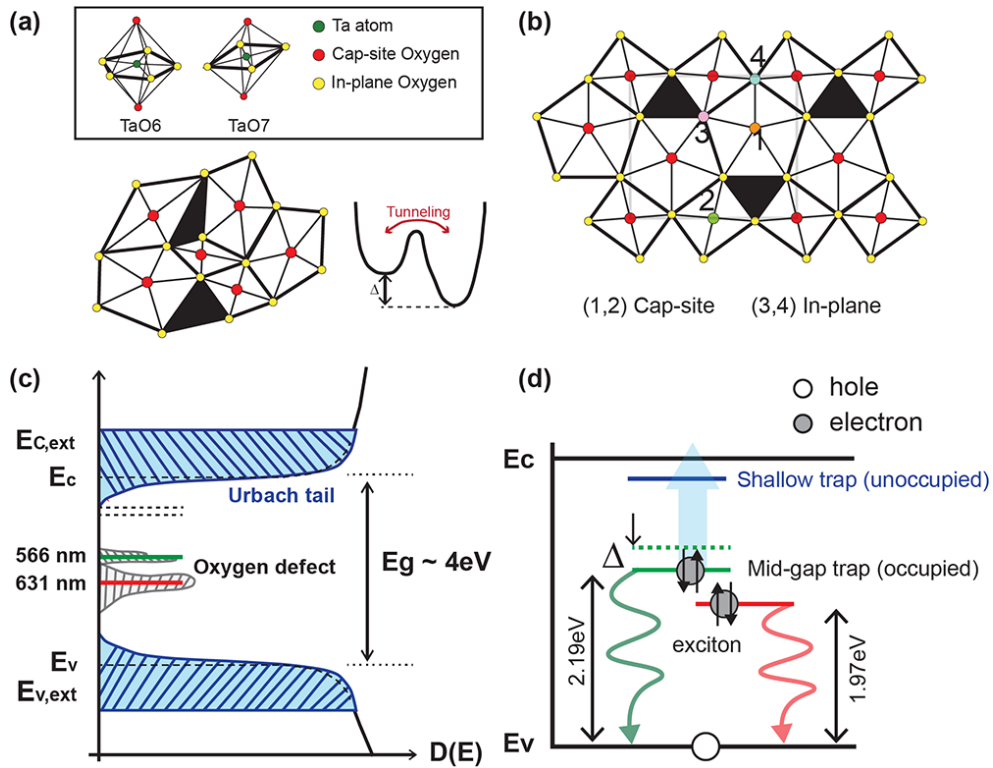


FIG. 1. Two-level systems and point defects in amorphous ($a\text{-Ta}_2\text{O}_5$) and crystalline tantalum pentoxide ($L\text{-Ta}_2\text{O}_5$). (a) $a\text{-Ta}_2\text{O}_5$. Long-range structural disorder can occur between configuration states. Such structural organization is phenomenologically mapped to a model of a thermally-activated tunnelling between two coupled potential wells. (b) $L\text{-Ta}_2\text{O}_5$ [19, 20]. (inset) Building block of $a\text{-Ta}_2\text{O}_5$ and $L\text{-Ta}_2\text{O}_5$. The relaxed crystal structure consists of several building blocks in corner (edge) sharing, with the Ta located at the center of the polyhedra. The inset displays the two polyhedra: Octohedra TaO_6 (left), and pentagonal bipyramid TaO_7 (right). Green sphere represents the tantalum atom, while the yellow (red) spheres are the oxygen atoms on the in-plane (cap) sites. The four dominant locations of oxygen vacancies are labeled with their indices and color coded. (c) Density of states (DOS) for $a\text{-Ta}_2\text{O}_5$. The Urbach tails (broadened oxygen defect states) are shown due to their long-wavelength (localized) structural disorder. E_c (E_v) is energy for the conduction (valence) band. The extended states of the conduction (valence) band formed by the long-range structural organizations are denoted as $E_{c,ext}$ ($E_{v,ext}$). (d) Possible optical transitions in in-plane oxygen vacancies in $a\text{-Ta}_2\text{O}_5$. The charge state is occupied in the mid-gap trap, and can be excited to the conduction band to generate photocurrent or to the shallow trap, which subsequently decays to the mid-gap trap. In photoluminescence (PL) spectroscopy, exciton generated near 2.19 eV by 450-nm pump laser experiences electron-hole pair recombination, generating PL photons at 566 nm (2.19 eV) and 631 nm (1.97 eV).

which have held the lowest AS ~ 1.1 ppm for any optical device ever since 1991.

II. NOISE MODEL OF AMORPHOUS TANTALA

Unlike crystalline structures with well-defined valence and conduction bands, amorphous dielectrics are characterized by the absence of long-range ordering (LRO). However, they have short-range ordering (SRO) at the molecular level, which opens a gap similar to crystalline materials. A prominent example of TLS defects in amorphous oxides is attributed to hydrogen in interstitial positions [21]. While they bond to the primary oxygen, they can also migrate to the neighbouring atoms. Following the TLS convention [1–4], this process can be captured by thermally activated tunnelling in an asymmetric double-

well potential, as shown for amorphous tantalum ($a\text{-Ta}_2\text{O}_5$) in Fig.1(a). As the hydrogen is the dominant background gas in ultra-high-vacuum environment, it is not always possible to prevent hydrogen contamination in thin film deposition and leads to an increased Brownian motion of the coatings.

The dynamics of TLS causes an internal friction to the dielectric media, which can be detected by the phonon scattering relaxation [22–25]. Namely, an internal friction is proportional to the tunnelling rate between the two potential well of the TLS modes. Mechanical loss of various metal oxide dielectrics have been extensively surveyed [25] and high-sample temperature and Ar-bombardment have been shown to be effective against oxygen deficiency that leads to internal friction in reactive IBS deposition [26]. While the microscopic origins of the TLS remain unclear, the compositional dis-

order by oxygen vacancies is a possible source of TLS for the mechanical loss in a-Ta₂O₅. Such a thermal noise of high-index tantala thin film ($n_H = 2.1$ at 852 nm) limits the sensitivity of present gravitational wave detectors [15] and the stability of optical references in an optical clocks [16, 17]. In the context of a-Ta₂O₅, mechanical dissipations can be alleviated by Titania-doping (Ti:Ta₂O₅) as network modifier [27, 28] and thermal annealing [9, 29]. Alternative high-index ($> n_H$) metal oxides are being developed with the objective of reducing the thicknesses of the dissipative coating layers [11]. Recent efforts include the development of crystalline mirrors to eliminate the structural TLS defects from the coating [8].

Beyond the thermal noise, the structural disorder introduced by oxygen defects in the LRO also contributes to optical losses of amorphous tantala [30]. Indeed, ab-initio studies confirm the microscopic origins of Urbach tails to structural topological organization caused by the relaxation in the presence of disorder [31]. As illustrated in Fig. 1(c), near the conduction band edge, the extended states become localized and their optical density of states $DOS(E)$ are broadened by an exponentially decaying Urbach tail $DOS(E) \propto e^{-(E_{gt}-E)/E_U}$, where E_U is the Urbach energy and $E_{gt} < E_{c,ext}$ characterizes the beginning of the Urbach tail for the extended states $E_{c,ext}$. The Urbach tail accompanies an optical absorption that decays from the extended states over the energy scale E_U , caused by the structural and thermal disorder in the system [31]. Such disorder creates a sub-gap broadening of the absorption edge that leads to an optical loss within E_U and detected by spectroscopic ellipsometry. With the band gap ~ 4.2 eV (302 nm) of tantala, the finite Urbach tail can be the dominant source of the optical absorption observed in high-finesse cavities in the UV and visible wavelengths < 450 nm.

Despite the amorphous nature of tantala, they also exhibit SRO at the molecular level, and the oxygen vacancies constitute microscopic point defects of the polycrystal. Similar to defect states in optical crystals (e.g., nitrogen vacancies in diamond), oxygen vacancies generate well-defined bound states (trap levels) and permit direct optical transitions. To understand the physics of these transitions and their intrinsic optical losses, let us briefly review the molecular structure of tantala and its oxygen defects. In tantala, there are 4 types of oxygen vacancies shown in Fig. 1(b) that depend on their locations. As shown in Fig. 1(b), the oxygen vacancies can arise from the absence of in-plane oxygen or cap oxygen, and they display qualitatively different optical behaviour from each other [31]. Since the cap oxygen vacancies are only shared by two polyhedra, the defect formation energy $E_d^{cap} \sim 4.9 - 5.3$ eV is considerably higher than in-plane oxygen vacancies $E_d^{in-plane} \sim 3.8 - 4.3$ eV [32], and oxygen defects are thereby more likely to relax into in-plane vacancies. Indeed, cap oxygen deficiencies (labeled as type 1 and 2 in Fig. 1(b)) create trap levels close to and buried within the conduction band, and are not relevant to our study. In-plane vacancies,

such as type 3 (4), is a deficiency of a single neutral oxygen that was originally shared with one (two) octohedra TaO₆ and two (one) pentagonal bipyramid TaO₇. Vacancies thereby leave behind the dangling bonds at the defect sites for the two electrons and form a well-defined two-level system (mid-gap trap and shallow trap) near the Fermi level hybridized by Ta (5d orbital) and O (2p orbital) within the bandgap of the tantala, which is optically addressable. Time-dependent density functional theory indicates that the occupied trap levels of type 3 and 4 defects are approximately located at 2.19 eV (566 nm) and 1.97 eV (631 nm) above the valence band E_v for dilute (non-interacting) defects [33], as shown in Fig. 1(d).

III. LONG-RANGE STRUCTURAL ORGANIZATION

While our primary focus is the reduction of optical loss, extensive research at LIGO [9–11] confirms the correlation between Urbach tail and internal friction in the metal oxides. Moreover, beyond its role as a network modifier, the titania doping is thought to quench the dangling bonds of excess oxygen. Indeed, oxygen vacancies of tantala can be compensated by Ti⁴⁺ ions as they substitute into the Ta⁵⁺ sites. Thermal annealing in oxygen rich environment has shown effective in the structural ordering of tantala. Reduction of unpaired electrons from the oxygen vacancies has been detected by a ¹⁷O MAS NMR spectra post thermal annealing [35]. We thereby apply a two-step post-treatment for the IBS mirrors: (1) Thermal annealing to relax the structural organization, followed by (2) a reactive O₂ plasma to reduce stoichiometric oxygen defects.

Bilayer quarter-wave stack (34-layers) of tantalum pentoxide and silica was deposited on a superpolished fused silica substrate with RMS surface roughness $\sim 0.25\text{\AA}$ by a reactive IBS with Ar⁺ bombardment. At the design wavelength 852 nm, the coating thickness for tantala (silica) is 162 (268) nm. The IBS mirrors were packaged in the cleanroom and annealed within a fused silica container. Based on Refs. [6, 10, 11], we perform an atmospheric thermal annealing at target temperature 450 °C in a muffle furnace, well below the critical temperature $T \sim 650^\circ\text{C}$ for the crystalline phase of tantala that yields an increased optical scattering loss by the grain boundaries [9, 29]. To relieve the coating stress, the ramping schedule was limited to 20 °C/hr and the sample was held at the target temperature for 12 hour. Following the annealing, the sample was treated by a reactive oxygen plasma (50 W at 50 kHz) at base pressure 10 mTorr and O₂ flow rate 5 scm.

To characterize the Urbach tail, we perform a spectroscopic ellipsometry across a broad spectral range for the tantala [38–40]. We independently characterize the coating thicknesses from transmission measurements with a laser-based spectrophotometer and measure the complex

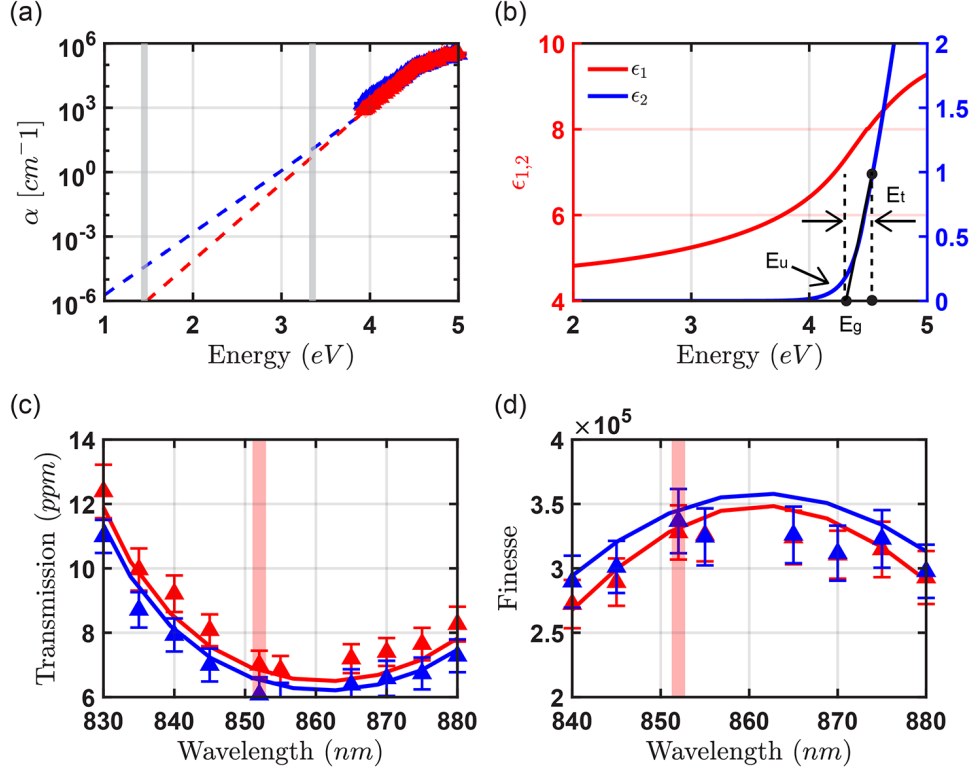


FIG. 2. Relaxing structural organizations by thermal and plasma annealing. (a) Measured absorption coefficient α of Ta₂O₅ from the ellipsometric data between 3.9 eV and 4.3 eV. The fitted curves are based on the Cody-Lorentz formula. (b) Reconstructed complex permittivities $\tilde{\epsilon} = \epsilon_1 + i\epsilon_2$ of tantalum. Only the data points for the complex permittivity before the annealing is shown. (c) Measured mirror transmission (T) based on loss partition in cavity ring-down spectroscopy [36]. The curves are computed from the transfer matrices with the ellipsometric determination of \tilde{n} for the coating layers. (d) Optical finesse of the Fabry-Perot cavity. The finesse is determined from the total loss $\mathcal{L} = T + AS$, where AS is the absorption-scatter loss. For the theory curve, in addition to the transfer matrices from the ellipsometric data, we use the absorption-scatter loss as a fitting parameter. Blue (red) data is measured before (after) the annealing. The annealing process consists of thermal annealing at atmospheric pressure, followed by a reactive O₂ plasma treatment. Urbach energy before (after) annealing is 150 meV (121) meV, and the gap energy before (after) annealing remains the same at 4.2 eV.

refractive index of IBS-grown silica as a reference. In particular, we detect the reflected fields r_p, r_s of the sample at incident angle 55° and reconstruct the ellipsometric angles (Ψ, Δ) where $\rho = r_p/r_s = \tan(\Psi) \exp(i\Delta)$ and r_p (r_s) is the reflected field projected to the p (s) polarization basis. From (Ψ, Δ), we can reconstruct the refractive index $\tilde{n}_H = n_H + ik_H$ of high-index dielectric layers from the optical transfer matrices, assuming known coating thickness. We thereby obtain the Urbach energy E_U by fitting the complex permittivity $\tilde{\epsilon} = \epsilon_1 + i\epsilon_2 = \tilde{n}^2$ using a Kramers-Kronig compliant Cody-Lorentz (CL) equation.

The CL model integrates the Lorentz oscillator with optical absorption near the extended states due to their structural organizations (such as the Urbach tail) and is

given by

$$\epsilon_1(\omega) - 1 = \frac{2}{\pi} \oint \frac{x\epsilon_2(x)}{x^2 - \omega^2} dx$$

$$\epsilon_2 = \begin{cases} \frac{E_{gt}G(E_g)L(E_g)}{E} \exp\left(\frac{E-E_{gt}}{E_u}\right), & 0 < E \leq E_{gt} \\ G(E)L(E), & E > E_{gt} \end{cases} \quad (1)$$

where $E_{gt} = (E_g + E_t)$ and gap energy E_g . For $E > E_{gt}$, ϵ_2 is a product of a variable band edge function $G(E) = \frac{(E-E_g)^2}{(E-E_g)^2 + E_p^2}$ and Lorentz oscillator $L(E) = \frac{AE_0\Gamma E}{(E^2 - E_0^2)^2 + \Gamma^2 E^2}$. For Lorentz oscillator function, E_0 is the peak energy for the Lorentz oscillator, A is the amplitude of the Lorentz oscillator, and Γ is the width of the Lorentz oscillator. The transition energy E_p defines the weighting factor between the Cody and the Lorentz models.

Fig. 2(a)-(b) show the spectroscopic ellipsometry measurements. Blue (red) data points are the measurement results before (after) the annealing. Before the anneal-

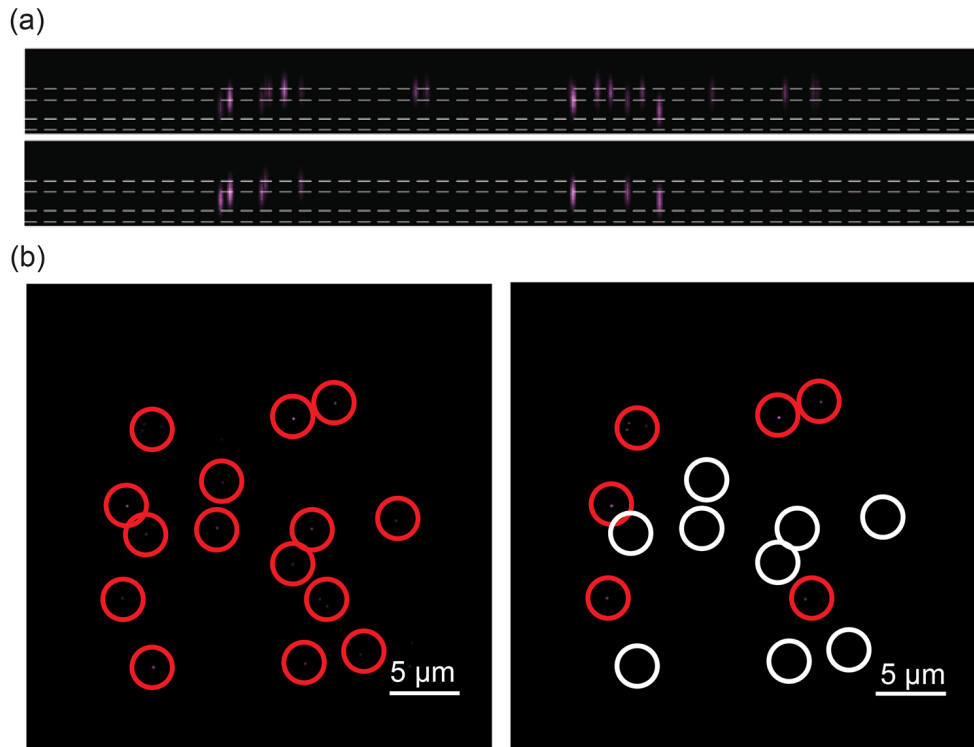


FIG. 3. Superresolution imaging of individual oxygen vacancies and laser-assisted annealing. (a) Cross-section of the reconstructed 3D image (depth image). The depth image before (after) laser-assisted annealing is shown on the top (bottom). The oxygen defects are mostly interfacial between tantala and silica (or vacuum). (b) Cross-section of reconstructed 3D image (transverse image). The individual oxygen vacancies are labeled with red circle before (after) the annealing on the left (right). The white circle indicates the position of oxygen defects that have been annealed. By inducing photoluminescence emission, 3D image of the individual defects is reconstructed from deconvolution microscopy that localizes the emitters to transverse (10 nm) and depth (75 nm) resolutions [37]. The point spread function is determined by a fluorescence bead on a test target.

ing, we observe gap energy $E_g \simeq 4.2 \pm 0.025$ eV and Urbach energy $E_U^{\text{initial}} = 150 \pm 17$ meV, in correspondence to other stoichiometric IBS tantala [9–11]. E_g^{initial} and E_U^{initial} are marked in the complex permittivities of Fig. 2(b). After the thermal annealing, we observe the structural relaxation accompanied by the decrease in the Urbach energy $E_U^{\text{anneal}} = 121 \pm 10$ meV. Fig. 2(b) displays the improved absorption coefficient α after annealing, extrapolated from the Urbach tail of the fitted CL model for the ellipsometric data between 3.9 – 4.3 eV.

To characterize the optical loss around 852 nm, we perform a loss partition of the cavity mirror by analyzing the transmitted and reflected intensities of the probe field during a cavity ring-down spectroscopy [36] (Section V). The finesse $\mathcal{F} = \pi/\mathcal{L}$ is computed based on the total loss $\mathcal{L} = T + AS$ of the mirror. We observe the decrease of absorption-scatter loss from $AS = 3.2 \pm 0.5$ ppm to $AS = 2.6 \pm 0.4$ ppm. Due to the improved stoichiometry of tantala, the refractive index n_H is reduced and results in higher transmission from $T = 6.1 \pm 0.5$ ppm to $T = 7.0 \pm 0.4$ ppm, leading to a minute reduction in the optical finesse (Fig. 2(d)). Other mirror samples consistently produce similar absorption-scatter loss $AS \sim 2 - 2.5$ ppm after the annealing, regardless of their initial AS . This

seems to suggest that our annealing process brings the tantala coating close to a stable optimal configuration.

A couple of remarks are in order. As a reference, we indicate two wavelengths for consideration in Fig. 2(a). The first is at 852 nm for our many-body QED platform [18]. In the NIR range, the reduced absorption from $\alpha \simeq 4.5 \times 10^{-5} \text{ cm}^{-1}$ to $< 10^{-6} \text{ cm}^{-1}$ does not have a meaningful contribution to the observed reduction of AS . Using the ellipsometric data, the expected absorption loss by the Urbach tail is only $AS \sim 0.02$ ppm for our mirror at 852 nm before the annealing. From AFM scans, we estimate the scattering loss $S \sim 0.14$ ppm with RMS surface roughness $\sim 0.25 \text{ \AA}$. On the other hand, for the near-UV cavity QED [41, 42], we anticipate that the absorption loss caused by the Urbach tail could be as high as $AS = 290$ ppm ($\alpha = 34 \text{ cm}^{-1}$) at 370 nm and $AS = 28$ ppm ($\alpha = 1.9 \text{ cm}^{-1}$) after annealing. These predictions are consistent to the absorption-scatter losses of high-finesse UV cavities in the literature [41, 42]. Our spectroscopic study of the Urbach tails indicates the relevance of long-range structural organization for short-wavelength high-finesse optical cavities.

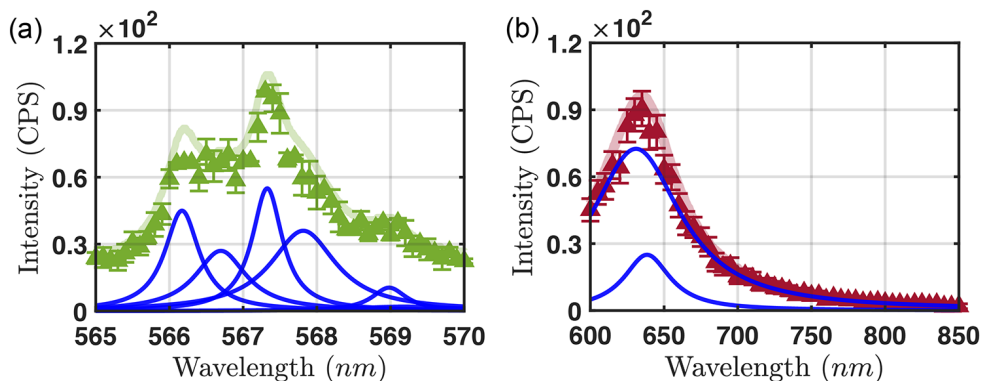


FIG. 4. Photoluminescence spectroscopy. Mid-gap trap levels are spectroscopically resolved. The spectrum is analyzed by the Voigt method and divided into multiple peaks with (a) center wavelengths near 567 nm and (b) 640 nm.

IV. PHOTOLUMINESCENCE SPECTROSCOPY AND SUPERRESOLUTION DEFECT IMAGING

Far away from the extended states of the conduction and valence bands (such as in the NIR range), optical losses of amorphous dielectrics are dominated by direct dipole-allowed transitions from (to) localized states to (from) extended states near the band edges. In particular, we focus on the in-plane oxygen vacancy levels, which form mid-gap trap levels near the Fermi level (See Fig. 1(c)-(d)). Because of the short-range nature, the emission linewidth E_d of photoluminescence is anticipated to be broad $E_d > E_U$, generating photons around 566 nm (2.19 eV) and 631 nm (1.97 eV). They may have sufficiently large dipole moment to dissipate the optical field in the cavity off-resonantly.

To develop a phenomenological picture, let us consider the TLS (radiative rate Γ) formed by the mid-gap trap $|g\rangle$ and the extended states $|e\rangle$ of the valence band with the TLS-cavity Hamiltonian

$$H_{\text{int}} = g_d(\hat{a}^\dagger \sigma_{ge} + \hat{a} \sigma_{eg}), \quad (2)$$

in the rotating frame of the cavity field's frequency, where g_d is the coupling rate of the cavity field to the defect and the TLS Hamiltonian $H_{TLS} = \Delta_d |e\rangle\langle e|$. For large detuning $\Delta_d \gg g_d, \Gamma$, the intrinsic cavity loss $\kappa_{\text{int}} \simeq (g_d/\Delta_d)^2 \Gamma$. We thereby anticipate the absorption loss of the cavity to slowly vary from the resonance with $\sim 1/\Delta_d^2$. Hence, in close spectral proximity to the defect states, the oxygen vacancies may have a decisive role in determining the absorption loss of ultra-high-finesse optical cavities at the few ppm level.

Indeed, there have been reports of mirror degradation by oxygen deficiencies under UHV environment [41–43]. In particular, Ref. [42] has claimed that the absorption-scatter loss AS from oxygen vacancy may be the primary contributor to the observed increase of AS when the optical cavity is exposed to UV field over a prolonged period. As discussed in Section II, the defect formation energies of in-plane oxygen vacancies greatly exceed the laser frequencies used in these experiments, and it is unlikely

that oxygen defects could have been formed by the lasers. Indeed, recent work [44] proposes the UV-enhanced deposition of hydrocarbons, generated from organic compounds, as the mechanism in which optical finesse in Ref. [42] decays under vacuum.

To make progress, we utilize a high-resolution UV optical microscope with $NA = 0.75$ and spatially resolve the individual oxygen defects on the IBS mirrors after the aforementioned annealing post-processing (Section III). We excite the mirror substrate with 450 nm pump with laser power between 5 – 30 mW to generate photoluminescence (PL) photons by exciton recombination near the mid-gap trap levels. We collect the PL photons on an EMCCD camera after a 550 nm edge-pass filter. We generate 61 images every 500 nm steps and the 3D image stack was processed with deconvolution algorithm [45] to reconstruct Fig. 3 with transverse (longitudinal) resolution 10 nm (75 nm).

As shown in Fig. 3(a), we observe that the oxygen defects are typically found at the interfacial layers between the tantala and silica. To further confirm that these images are the result of the PL from oxygen defect states, we construct the spectrum of the PL via a high-resolution spectrograph with resolution 0.1 nm, as shown in Fig. 4. In particular, we are able to resolve both mid-gap trap levels at ~ 567 nm and ~ 647 nm, consistent to Ref. [46]. In particular, we observe that the PL signal from the trap level of type 3 vacancy can extend down to 852 nm. This implies that optical excitations between the defect levels may lead to optical absorption at the NIR range. Motivated by these measurements and Refs. [42, 47, 48], we perform atmospheric laser-assisted annealing of the tantala with a 10-mW UV laser at 380 nm focused to spot size $20\mu\text{m}$. In Fig. 3, we demonstrate that out of the 18 defects, 9 defects can be recovered with this method. We find that the laser annealing is only effective for oxygen defects on the mirror surface, which hints a potential mechanism of laser-assisted stoichiometry for vacancies exposed to ambient oxygen. Further study is required to examine the physical mechanism behind the laser-assisted annealing.

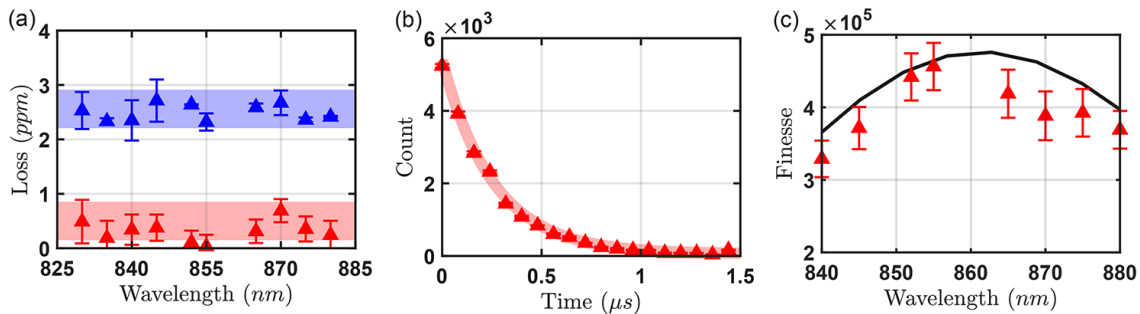


FIG. 5. Loss partition in cavity ring-down spectroscopy. (a) Absorption-scatter loss before (blue) and after laser annealing (red). At the design wavelength (852 nm), we obtain $AS = 0.1 \pm 0.2$ ppm after laser annealing. (b) Cavity ring-down spectroscopy. We observe the cavity decay rate $\kappa/2\pi = 130$ kHz after laser annealing. (c) Ultra-high-finesse \mathcal{F} optical cavity. Together with the results of (a) and transmission loss $T = 6.1 \pm 0.5$ ppm at 852 nm, we obtain cavity finesse $\mathcal{F} = (4.4 \pm 0.3) \times 10^5$ after laser annealing.

V. ULTRA-HIGH-FINESSE OPTICAL CAVITY

By spatially localizing and curing individual defects, we systematically construct an ultra-high-finesse optical cavity with the mode area positioned near defect-free regions. To perform the loss partition, we follow the protocol of Ref. [36]. Namely, we detect both the transmitted (P_t) and reflected (P_r) probe power during a cavity ring-down spectroscopy. Along with the cavity decay rate $\sim \kappa$, this method allows us to obtain

$$\mathcal{F} = \frac{\pi}{\mathcal{L}} = \frac{FSR}{2\kappa}, \quad (3)$$

$$AS = \frac{2\pi\kappa}{FSR} \left(\frac{P_r - P_t}{P_r + P_t} \right), \quad (4)$$

$$T = \frac{2\pi\kappa}{FSR} \left(\frac{2P_t}{P_r + P_t} \right), \quad (5)$$

where the free-spectral range (FSR) is $FSR = c/2L_c$ and the total loss is $\mathcal{L} = AS + T$. In our measurement, we directly probe the $FSR = 116.52 \pm 0.03$ GHz of the ~ 1.3 mm-long cavity with stabilized lasers on a wavemeter. To probe the optical cavity, we use a narrow-linewidth (~ 100 Hz) Ti:S laser for the cavity ring-down spectroscopy. The probe field is extinguished within 10 ns. The two Geiger-mode single-photon APDs are calibrated with intensity stabilized laser, and the uncertainties of the passive losses of the optical setup are accounted as systematic errors in all data.

Fig. 5 presents the loss partitions of the optical cavity for many-body QED experiment [18]. The test cavity is constructed in a class-10 cleanroom environment. For the post-processed mirror samples with the defect free-region near the center, the cavity mode is imaged through the mirror with the resolution $\sim 3\mu m$ limited by the spherical aberrations. The cavity ring-down spectroscopy is performed within a vacuum chamber with moderate pressure ~ 1 mTorr to avoid the contributions from the atmospheric losses. In Fig. 5(a), we demonstrate that the post-processing by laser-annealing can make tangible im-

AS Loss (before)	T Loss (before)	AS Loss (after)	T Loss (after)
3.3 ± 0.5 ppm	6.1 ± 0.5 ppm	0.1 ± 0.2 ppm	7.0 ± 0.4 ppm

TABLE I. Summary of loss partitions at 852 nm for ultra-low-loss dielectric mirrors before and after the post-processing (thermal and laser annealing stages). Absorption-scatter (AS) and transmission (T) losses are partitioned with the cavity ring-down spectroscopy based on the method of Ref. [36].

provement in the absorption-scatter loss of thermally annealed sample. We observe that the absorption-scatter loss at 852 nm is reduced from $AS = 2.6 \pm 0.4$ ppm to a record-low $AS = 0.1 \pm 0.2$ ppm, reaching the physical limits of the scattering loss $S \sim 0.14$ ppm of the mirror with the RMS surface roughness $\sim 0.25\text{\AA}$ determined from atomic force microscopy. The summary of the loss partitions for the original mirrors and the final post-processed mirrors are shown in Table I.

VI. CONCLUSION

In conclusion, we have provided the first microscopic study that connects structural deformation and optical losses of amorphous media. We investigated the key role of oxygen vacancies in tantala for the long-range and short-range structural deformations. At the level of LRO, the dislocation and disorder of amorphous tantala have an indirect quantitative contribution to the absorption losses by the Urbach tails for short-wavelength optical resonators. In the SRO regime, we have investigated the optical transitions between the trap levels of in-plane oxygen vacancies at the individual defect level by photoluminescence spectroscopy and deconvolution microscopy. For long-wavelength ultra-high-finesse optical resonators, optical losses are dominated by direct optical excitations of the defect states. By developing a novel laser-annealing technique, we provide a microscopic tool to recover stoichiometry at the atomistic level.

Utilizing these understandings, we report the realization of the ultra-high-finesse optical cavity for many-body QED experiments with finesse $\mathcal{F} = (4.4 \pm 0.3) \times 10^5$ [18], where losses are only limited by the surface qualities over a designated cavity mode volume. Importantly, our measurement of absorption-scatter (AS) loss $AS = 0.1 \pm 0.2$ ppm improves upon the landmark achievement by Rempe *et al.*, which have held the world record $AS = 1.1$ ppm for any optical device over the past three decades [12]. Stated differently, we realize a nearly defect-free amorphous optical system, whose optically active atomistic defects could be counted over a region $\sim 1000 \mu\text{m}^2$.

ACKNOWLEDGMENTS

This research was supported by the Canada Foundation for Innovation (CFI), the Compute Canada, the

IDEX Bordeaux, the Innovation, Science and Economic Development Canada (ISED), the KIST Institutional Program, the Natural Sciences and Engineering Research Council of Canada (NSERC), the National Research Council Canada, the NVIDIA, and the Ontario Ministry of Research and Innovation. The University of Waterloo's Quantum-Nano Fabrication and Characterization Facility (QNFCF) was used for part of this work. This infrastructure is supported by CFREF-TQT, CFI, ISED, the Ontario Ministry of Research & Innovation, and Mike & Ophelia Lazaridis. We acknowledge the CMC Microsystems for the CAD tools and fabrication services.

-
- [1] W. A. Phillips, Tunneling States in Amorphous Solids. *J. Low Temp. Phys.* **7**, 351 (1972).
- [2] P. W. Anderson, B. I. Halperin and C. M. Varma, Anomalous low-temperature thermal properties of glasses and spin glasses. *The Philosophical Magazine: A Journal of Theoretical Experimental and Applied Physics.* **25**, 1 (1972).
- [3] A. O. Caldeira, and A. J. Leggett, Quantum tunnelling in a dissipative system. *Ann. Phys.* **149**, 374 (1983).
- [4] W. A. Phillips, Two-level states in glasses. *Rep. Prog. Phys.* **50**, 1657 (1987).
- [5] H. Sawada and K. Kawakami, Electronic structure of oxygen vacancy in Ta_2O_5 . *J. Appl. Phys.* **86**, 956 (1999).
- [6] N. Kim and J. F. Stebbins, Effects of annealing on the structure of ion beam sputtered amorphous tantalum oxide oxygen 17 NMR spectra and relaxation times. *J. Non-Crystal. Solids* **378**, 158 (2013).
- [7] I. W. Martin *et al.*, Low temperature mechanical dissipation of an ion-beam sputtered silica film. *Class. Quant. Grav.* **31**, 035019 (2014).
- [8] G. D. Cole, W. Zhang, M. J. Martin, J. Ye, M. Aspelmayer, Tenfold reduction of Brownian noise in high-reflectivity optical coatings. *Nature Photon.* **7**, 644 (2013).
- [9] A. Amato *et al.* High-Reflection Coatings for Gravitational-Wave Detectors: State of The Art and Future Developments. *J. Phys.: Conf. Ser.* **957**, 012006 (2018).
- [10] A. Amato *et al.*, Optical properties of high-quality oxide coating materials used in gravitational-wave advanced detectors. *J. Phys.* **2**, 035004 (2019).
- [11] A. Amato *et al.* Observation of a correlation between internal friction and Urbach energy in amorphous oxides thin films. *Sci. Rep.* **10**, 1670 (2020).
- [12] G. Rempe, R. J. Thompson, H. J. Kimble, and R. Lalezari, Measurement of ultralow losses in an optical interferometer. *Optics Lett.* **17**, 363 (1992).
- [13] M. Brownnutt *et al.* Ion-trap measurements of electric-field noise near surfaces. *Rev. Mod. Phys.* **87**, 1419 (2015).
- [14] C. Müller *et al.* Towards understanding two-level-systems in amorphous solids: insights from quantum circuits. *Rep. Prog. Phys.* **82**, 124501 (2019).
- [15] G. Harry *et al.* Thermal noise from optical coatings in gravitational wave detectors. *Appl. Opt.* **45**, 1569 (2006).
- [16] T. Kessler *et al.* A sub-40-mHz-linewidth laser based on a silicon single-crystal optical cavity. *Nature Photon* **6**, 687 (2012).
- [17] D. Andrew *et al.* Optical atomic clocks. *Rev. Mod. Phys.* **87**, 637 (2015).
- [18] H. R. Kong, J. Taylor, Y. Dong, and K. S. Choi, Melting a Rydberg ice to a topological quantum spin liquid with cavity vacuum fluctuation. In preparation.
- [19] N. C. Stephenson and R. S. Roth, Structural systematics in the binary system $\text{Ta}_2\text{O}_5\text{-WO}_3$. V. The structure of the low-temperature form of Tantalum Oxide $L\text{-Ta}_2\text{O}_5$. *Acta Cryst.* **B27**, 1037 (1971).
- [20] Y. Yang and Y. Kawzoe, Prediction of new ground state crystal structure of Ta_2O_5 . *Phys. Rev. Mat.* **2**, 034602 (2018).
- [21] L. Gordon *et al.* Hydrogen bonds in Al_2O_3 as dissipative two-level systems in superconducting qubits. *Sci. Rep.* **4**, 7590 (2014).
- [22] D. G. Cahill, and J. E. van Cleve, Torsional oscillator for internal friction data at 100 kHz. *Rev. Sci. Instr.* **60**, 2706 (1989).
- [23] X. Liu and R. O. Pohl, Low-energy excitations in amorphous films of silicon and germanium. *Phys. Rev. B* **58**, 9067 (1998).
- [24] J. Classen, T. Burkert, C. Enss, and S. Hunklinger, Anomalous frequency dependence of the internal friction of vitreous silica. *Phys. Rev. Lett.* **84**, 2176 (2000).
- [25] R. O. Pohl, X. Liu, and E. Thompson, Low-temperature thermal conductivity and acoustic attenuation in amorphous solids. *Rev. Mod. Phys.* **74**, 991 (2002).
- [26] X. Liu, D. R. Queen, T. H. Metcalf, J. E. Karel, and F. Hellman, Hydrogen-free amorphous silicon with no tunneling states. *Phys. Rev. Lett.* **113**, 025503 (2014).

- [27] L. Manchanda *et al.* Multi-component high-K gate dielectrics for the silicon industry. *Micro. Eng.* **59** 351 (2001).
- [28] E. Atanassova, A. Paskaleva and D. Spassov, Doping of Ta₂O₅ as a way to extend its potential for DRAM applications. *2010 27th International Conference on Microelectronics Proceedings*, 427 (2010).
- [29] G. Vajente *et al.* Effect of elevated substrate temperature deposition on the mechanical losses in tantalum thin film coatings. *Class. Quantum Grav.* **35**, 075001 (2018).
- [30] A. S. Markosyan *et al.* Study of spontaneous and induced absorption in amorphous Ta₂O₅ and SiO₂ dielectric thin films. *J. Appl. Phys.* **113**, 133104 (2013).
- [31] Y. Pan, M. Zhang, and D. A. Drabold, Topological and topological-electronic correlations in amorphous silicon. *Journal of Non-Crystalline Solid* **354**, 3480 (2008).
- [32] Y. Yang, H.-H. Nahm, O. Sugino, and T. Ohno, Electronic structures of oxygen-deficient Ta₂O₅. *AIP Adv.* **3**, 042101 (2013).
- [33] R. Ramprasad, First principles study of oxygen vacancy defects in tantalum pentoxide. *J. App. Phys.* **94**, 5609 (2003).
- [34] E. Atanassova *et al.* Electrical characteristics of Ti-doped Ta₂O₅ stacked capacitors. *Thin Solid Films.* **516**, 8684 (2008).
- [35] N. Kim and J. F. Stebbins, Structure of amorphous tantalum oxide and titania-doped Tantalum: ¹⁷O NMR results for sol-gel and ion-beam-sputtered materials. *Chem. Mat.* **23**, 3460 (2011).
- [36] C. J. Hood, H. J. Kimble, and J. Ye, Characterization of high-finesse mirrors: Loss, phase shifts, and mode structure in an optical cavity. *Phys. Rev. A* **64**, 033804 (2001).
- [37] W. Z. He *et al.* Image deconvolution for defected crystals in field-emission high-resolution electron microscopy. *Ultramicroscopy* **70** 1 (1997).
- [38] F. Urbach, The long-wavelength edge of photographic sensitivity and of the electronic absorption of solids. *Phys. Rev.* **92** 1324 (1953).
- [39] H. Fujiwara, Spectroscopic ellipsometry: principles and applications. *John Wiley & Sons*, (2007).
- [40] G.D. Cody *et al.* Disorder and the optical-absorption edge of hydrogenated amorphous silicon. *Phys. Rev. Lett.* **47** 1480 (1981).
- [41] B. Brandstatter *et al.* Integrated fiber-mirror ion trap for strong ion-cavity coupling. *Rev. Sci. Instrum.* **84**, 123104 (2013).
- [42] D. Gangloff *et al.* Preventing and reversing vacuum-induced optical losses in high-finesse tantalum (V) oxide mirror coatings. *Opt. Express* **23**, 18014 (2015).
- [43] M. Cetina *et al.* One-dimensional array of ion chains coupled to an optical cavity. *New J. Phys.* **15** 053001 (2013).
- [44] J. Schmitz, H. Meyer, and M. Köhl, Ultraviolet fabry-perot cavity with stable finesse under ultra-high vacuum conditions. *Rev. Sci. Inst.* **90**, 063102 (2019).
- [45] P. Wendykier and J. G. Nagy, Parallel Colt: A High-Performance Java Library for Scientific Computing and Image Processing. *ACM Trans. Math. Softw.* **37**, 3 (2010).
- [46] R. S. Devan *et al.* High room-temperature photoluminescence of one-dimensional Ta₂O₅ nanorod arrays. *Nanotech.* **20**, 445708 (2009).
- [47] J.-Y. Zhang *et al.* Ultraviolet annealing of tantalum oxide films grown by photo-induced chemical vapour deposition. *J. Phys. D: Appl. Phys.* **32**, L91 (1999).
- [48] R. M. Fleming *et al.* Defect dominated charge transport in amorphous Ta₂O₅ thin films. *J. App. Phys.* **88**, 850 (2000).